Intrinsic exciton-state mixing and nonlinear optical properties in transition metal dichalcogenide monolayers

M. M. Glazov[*] and L. E. Golub

Ioffe Institute, St. Petersburg 194021, Russia

G. Wang, X. Marie, T. Amand, and B. Urbaszek

Université de Toulouse, INSA-CNRS-UPS, LPCNO, 31077 Toulouse, France

Optical properties of transition metal dichalcogenides monolayers are controlled by Wannier-Mott excitons forming a series of $1s, 2s, 2p, \ldots$ hydrogen-like states. We develop the theory of the excited excitonic states energy spectrum fine structure. We predict that p- and s-shell excitons are mixed due to the specific D_{3h} point symmetry of the transition metal dichalcogenide monolayers. Hence, both s- and p-shell excitons are active in both single- and two-photon processes, providing an efficient mechanism of second harmonic generation. The corresponding contribution to the nonlinear susceptibility is calculated.

I. INTRODUCTION

Transition metal dichalcogenide monolayers (TMD MLs) such as MoS_2, $MoSe_2$, WS_2, WSe_2, etc., are prototypical two-dimensional (2D) semiconductors with direct band gaps of the order of 2 eV at the Brillouin zone edges [1–5]. Optical properties of these systems are mainly governed by the Coulomb correlated electron-hole pairs, excitons [6,7]. Due to relatively large effective masses of the electrons and holes and rather weak screening of the Coulomb interaction in 2D systems [8,9], excitons are highly stable in TMD MLs: The predicted [10–14] and observed [15–20] exciton binding energies amount to $\sim$500 meV. The oscillator strengths of excitons in TMD MLs are also much higher as compared with conventional 2D structures based, e.g., on GaAs [21–25]. Just like the direct Coulomb interaction, the electron-hole exchange interaction in TMD MLs is also stronger than in conventional semiconductors [26–29]. It controls the spin and valley dynamics of excitons in a wide range of temperatures [30]; see for review Ref. [31] and references therein.

Excitons also play a crucial role in nonlinear optical properties, particularly, in two-photon absorption and second harmonic generation in 2D TMD [16,18,20,32–34]. The nonlinear susceptibility is enhanced in the vicinity of excitonic resonances due to redistribution of the oscillator strength from a continuum to bound electron-hole pair states [20,34,35]. It is usually assumed that the s-shell exciton states are active in single-photon processes, while p-shell excitons are optically active in two-photon processes [36,37]. The energies of the ground, $1s$, and excited $2s, 2p, \ldots$ excitonic states strongly differ from the hydrogenic series due to unusual screening in TMD MLs [17]. Moreover, for the same reason, in TMD MLs the "accidental" Coulomb degeneracy of excited excitonic states is lifted. As a result, the fine structure of the excited, e.g., $2p$-exciton, states in TMD MLs has become topical nowadays, in particular, in view of possible manifestations of the Berry curvature effect [38,39].

Here we demonstrate that the s- and p-shell excitonic states are mixed in TMD monolayers. We present a detailed theory of the fine structure of excited excitonic states in TMD MLs, including the symmetry analysis and the microscopic theory. The microscopic mechanisms of the mixing are uncovered and a detailed model is developed within the $\boldsymbol{k} \cdot \boldsymbol{p}$ formalism. The mixing is shown to be quite substantial; for example, the coupling constant of $2s$- and $2p$-shell states is estimated to be in the range from tenths to several meV. In particular, the mixing makes s-shell states active in the two-photon absorption and also contributes to the second harmonic generation in TMD MLs. The excitonic contributions to the two-photon absorption and nonlinear susceptibility responsible for the second harmonic generation are calculated.

II. SYMMETRY ANALYSIS

The exciton basic wave functions in semiconductors can be recast as products of the two-particle envelope and Bloch functions. For the exciton freely propagating in the TMD ML plane with the center-of-mass wave vector $\boldsymbol{K}$, the wave function Ψ reads [31]

$$\Psi_{\boldsymbol{K};\nu,\mu}(\boldsymbol{\rho}_e, \boldsymbol{\rho}_h) = \exp{(i\boldsymbol{K}\boldsymbol{R})}\Phi_\nu(\boldsymbol{\rho})\mathcal{U}_\mu(\boldsymbol{\rho}_e, \boldsymbol{\rho}_h). \quad (1)$$

The exciton state is characterized by quantum numbers $\nu = 1s, 2s, 2p, \ldots$ denoting the hydrogen-like relative motion states and μ enumerating the band states, $\Phi_\nu(\boldsymbol{\rho})$ is the relative motion wave function, and $\mathcal{U}_\mu(\boldsymbol{\rho}_e, \boldsymbol{\rho}_h)$ is the two-particle Bloch function. Here $\boldsymbol{\rho}_e$, $\boldsymbol{\rho}_h$ are the electron and hole in-plane coordinates, respectively, $\boldsymbol{\rho} = \boldsymbol{\rho}_e - \boldsymbol{\rho}_h$ is the relative coordinate, $\boldsymbol{R} = (m_e\boldsymbol{\rho}_e + m_h\boldsymbol{\rho}_h)/(m_e + m_h)$ is the center-of-mass position vector, m_e (m_h) are the electron (hole) effective masses, and the normalization area is set to unity. In what follows we focus on the states with $\boldsymbol{K} = 0$ and restrict ourselves with optically active Bloch states denoted as $\mu = \pm 1$ (active in $\sigma^\pm$ polarizations, respectively) or, alternatively, as $\mu = x, y$, where x and y denote orientation of oscillating dipole moment in the Cartesian coordinate frame with the in-plane axes x, y and the normal to the TMD ML z. The "dark" excitons with opposite spins of the electron and the hole which

———————
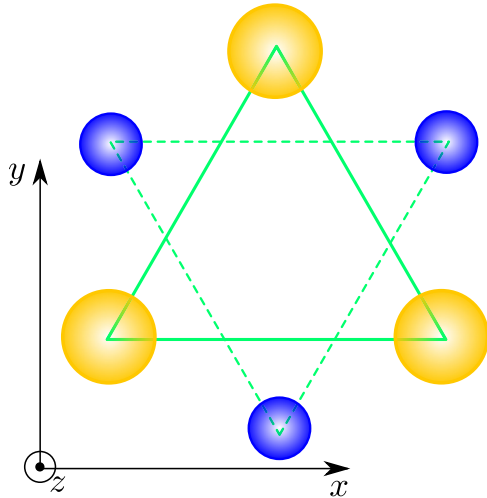[*]Corresponding author: glazov@coherent.ioffe.ru

FIG. 1. Top view of atomic arrangement in a TMD ML. Yellow circles show positions of the transition metal atoms, blue circles show the projection of chalcogen atoms on the horizontal plane. Green lines are guides showing nonequivalent triangles responsible for the overall D_{3h} point symmetry of the ML.
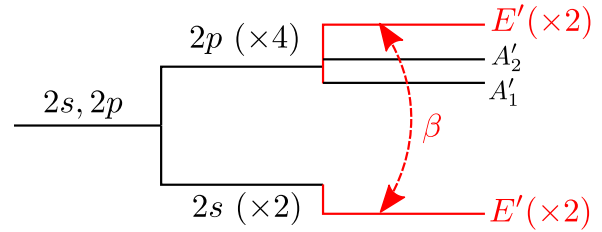

FIG. 2. Sketch of the $2s$- and $2p$-shell exciton fine structure. The splitting between the $2p$ quadruplet and $2s$ doublet (accounting for the Bloch functions orbital degeneracy) arises due to the specific screening of the Coulomb interaction in TMD MLs. The splitting of the $2p$ quadruplet arises in D_{3h} point symmetry and the $2p$ (E') states are mixed with the $2s$ (E') states. The order of lines is arbitrary and the splittings are shown not to scale.

are weakly optically active in the polarization perpendicular to the ML plane are disregarded [26,40,41].

The point symmetry of the TMD ML is D_{3h}, in the chosen coordinate frame z is the threefold rotation axis and y is (one of three) twofold in-plane rotation axes, the horizontal reflection plane $\sigma_h \parallel (xy)$, one of three vertical reflection planes is $\sigma_v \parallel (yz)$, and two remaining planes can be obtained from σ_v by the rotation through the angles $\pm 2\pi/3$ around the z axis. The set of axes and atomic arrangement is illustrated in Fig. 1. In accordance with the general theory, the exciton eigenstates in a TMD ML transform according to irreducible representations of the D_{3h} point group [36].

The symmetry of the exciton basic state is, in accordance with Eq. (1), described by the product of irreducible representations corresponding to the relative motion wave function and Bloch function. Notably, the symmetry of the two-dimensional envelope function $\Phi_\nu(\boldsymbol{\rho})$ can be either A_1' or Γ_1 in the notations of Ref. [42] (the identical representation, s shell) or E' or Γ_6 (the in-plane vector components, p shells). In fact, all other 2D hydrogen-like states transform by reducible representations that are combinations of those two; for instance, d-shell excitonic states (with the angular momentum z component being ± 2) transform according to E', because in the D_{3h} point symmetry the pair of coordinates (x,y) transform exactly as the second-order combinations $(2xy, x^2 - y^2)$. The Bloch functions $\mathcal{U}_{x,y}$ of the optically active states transform according to the two-dimensional irreducible representation E'. Hence, accounting for the Bloch function, the s-shell excitons transform according to the irreducible two-dimensional representation

$$\mathcal{D}_s = A_1' \times E' = E', \tag{2}$$

while p-shell excitonic states transform according to the reducible representation

$$\mathcal{D}_p = E' \times E' = A_1' + A_2' + E'. \tag{3}$$

Equation (3) demonstrates that, accounting for the point symmetry of the TMD ML, the p-shell quadruplet is split into two nondegenerate sublevels (A_1', A_2') and the twofold degenerate level E' with the eigenfunctions (the normalization constants are omitted for brevity)

$$A_1': \quad \Phi_{p_x}\mathcal{U}_x + \Phi_{p_y}\mathcal{U}_y, \tag{4a}$$

$$A_2': \quad \Phi_{p_x}\mathcal{U}_y - \Phi_{p_y}\mathcal{U}_x, \tag{4b}$$

$$E'(1): \quad \Phi_{p_x}\mathcal{U}_y + \Phi_{p_y}\mathcal{U}_x, \tag{4c}$$

$$E'(2): \quad \Phi_{p_x}\mathcal{U}_x - \Phi_{p_y}\mathcal{U}_y. \tag{4d}$$

The splitting between the $2p$ states transforming according to E' and ($A_1' + A_2'$) was discussed in Refs. [37–39,43]. It has been demonstrated on the basis of effective Hamiltonian analysis [38,39] and microscopic calculations [43] that the $2p$ states with angular momentum components ± 1, $\Phi_{p_{\pm 1}} \propto \Phi_{p_x} \pm i\Phi_{p_y}$ are split within a given valley, while the time-reversal symmetry implies the equality of $\Phi_{p_{\pm 1}}$ and $\Phi_{p_{\mp 1}}$ states in $\boldsymbol{K}_+$ and $\boldsymbol{K}_-$ valleys, respectively. Equation (4) demonstrates that the doublet ($A_1' + A_2'$) is further split in TMD MLs. This splitting between A_1' and A_2' as well as the mixing between s-shell and p-shell states (see below) was not addressed. The fine structure of p-shell exciton states is illustrated in Fig. 2 for the particular example of $2p$ excitons. The basic functions (4) can be represented in an alternative form in the basis of states with a given angular momentum z component ± 1 as $\Phi_{p_{+1}}\mathcal{U}_{-1} \pm \Phi_{p_{-1}}\mathcal{U}_{+1}$, where the top (bottom) sign corresponds to an A_1' (A_2') irreducible representation, and as $\Phi_{p_{+1}}\mathcal{U}_{+1}$, $\Phi_{p_{-1}}\mathcal{U}_{-1}$ for two basic functions of the E' irreducible representation. The latter functions formally correspond to the total angular momentum component being ± 2 and, since the threefold rotation leaves third angular harmonics invariant, these functions transform exactly as the states with the angular momentum components ∓ 1, respectively. The states A_1' and A_2' are, respectively, symmetrized and antisymmetrized combinations of the basic functions with the total angular momentum component being 0.

Moreover, it follows from Eqs. (2) and (3) that the s-shell excitonic states and the combination of Eqs. (4c) and (4d) of the p-shell states transform according to the same irreducible representation E' of the D_{3h} point group. Therefore, the mixing of these states is possible. In particular, the p-shell

state combination $\Phi_{p_x}\mathcal{U}_x - \Phi_{p_y}\mathcal{U}_y$ mixes with $\Phi_s\mathcal{U}_y$ and the $\Phi_{p_x}\mathcal{U}_y + \Phi_{p_y}\mathcal{U}_x$ mixes with $\Phi_s\mathcal{U}_x$. In the basis of the states with given components of the total angular momentum, the mixing involves the pairs

$$\Phi_{p_{+1}}\mathcal{U}_{+1} \leftrightarrow \Phi_s\mathcal{U}_{-1}, \quad \Phi_{p_{-1}}\mathcal{U}_{-1} \leftrightarrow \Phi_s\mathcal{U}_{+1}. \tag{5}$$

This mixing makes p-shell states optically active. Note that this mixing is absent in the axially symmetric approximation. For given principal quantum numbers n and m of the s- and p-shell states, the mixing is described by a single parameter β_{nm}. To illustrate this mixing in more detail we focus on the states with the principal quantum numbers $n = m = 2$. We note that for purely Coulomb potential the $2s$ and $2p$ levels are degenerate. This so-called "accidental" degeneracy is lifted for the effective electron-hole interaction potential in the TMD ML, which accounts for specifics of the screening. The spin-orbit interaction as well as nonparabolicity of the single-particle energy spectrum can also contribute to the s-p exciton splitting [37–39,44]. To the best of our knowledge this expected splitting has not been measured so far. The effective Hamiltonian of $2s/2p$ excitons can be represented by

$$\mathcal{H}_{2X} = \begin{pmatrix} E_{2s} & 0 & 0 & 0 & \beta & 0 \\ 0 & E_{2s} & 0 & 0 & 0 & \beta \\ 0 & 0 & E_{2p}^{(A_1')} & 0 & 0 & 0 \\ 0 & 0 & 0 & E_{2p}^{(A_2')} & 0 & 0 \\ \beta & 0 & 0 & 0 & E_{2p}^{E'} & 0 \\ 0 & \beta & 0 & 0 & 0 & E_{2p}^{E'} \end{pmatrix}. \tag{6}$$

Here the basic functions are chosen in the following order: $2s$; $E'(1)$, $2s$; $E'(2)$, $2p$; A_1', $2p$; A_2', $2p$; $E'(1)$ $2p$; $E'(2)$. The diagonal energies E_{2s}, $E_{2p}^{A_1'}$, etc., denote exciton energies neglecting the s-p mixing (but, e.g., accounting for lifting of the Coulomb degeneracy and $p_{\pm 1}$ states splitting within a given valley), and $\beta \equiv \beta_{22}$ is the mixing parameter. Obviously, the effective Hamiltonians for the multiplets with different principal quantum numbers have the same form with different values of parameters; the mixing is symmetry allowed between any n and m.

III. MICROSCOPIC ORIGIN OF s-p EXCITON MIXING

In this section we develop the microscopic model of the s-p exciton mixing. The splitting of s-shell and p-shell excitonic states for the given principal quantum number n has been discussed in the literature in detail; see Ref. [37] and references therein. The E' doublet of p-shell states and the two states A_1', A_2' are split as a result of the $\boldsymbol{k} \cdot \boldsymbol{p}$ interaction and the band mixing [38,39]. This splitting as well as the splitting between A_1' and A_2' p-shell excitons (studied for axially symmetric quantum dots in Ref. [45]) is allowed in the axially symmetric model and it does not rely on specific features of the TMD symmetry and band structure. In contrast, the mixing of the p- and s-shell states requires accounting for the symmetry reduction from the axial down to the threefold symmetry. Note that in TMD MLs the bright exciton Bloch function involves the electron state in the $\boldsymbol{K}_\pm$ valley and the hole state in the $\boldsymbol{K}_\mp$ valley; see Ref. [31] and the text below for details. Therefore, since the mixing involves the pairs, Eq. (5), where the electron and hole in the initial and final states should swap valleys,

the coupling between p- and s-shell excitons is a combined effect of the $\boldsymbol{k} \cdot \boldsymbol{p}$ mixing of the energy bands and the electron-hole interaction. Both the short- and long-range parts of the electron-hole exchange interaction may enable simultaneous intervalley transfer of the electron and the hole [26,27]. Below we calculate two contributions to the mixing parameter $\beta = \beta_s + \beta_l$ related to both exchange interaction mechanisms: the short-range contribution, β_s, in Sec. III B and the long-range one, β_l, in Sec. III C.

In what follows we present the model of the exciton mixing based on the following steps. First, we introduce the envelope functions $\Phi_\nu(\boldsymbol{\rho})$, which can be calculated within the effective mass method as, e.g., in Ref. [17]. Second, we take into account the first-order $\boldsymbol{k} \cdot \boldsymbol{p}$ mixing between the different bands, which results in the mixing of the s- and p-shell excitonic states within a given valley (Sec. III A). Third, the short- and long-range parts of the exchange interaction are taken into account to derive the mixing between the excitons in different valleys (Secs. III B and III C). Hereafter we rely on the following relation between characteristic energies in the system:

$$E_g \gg E_b \gg \delta_l \gg E_{\text{exch}}. \tag{7}$$

Here E_g is the free particle band gap, E_b is the exciton binding energy, and δ_l is the energy splitting of the excitonic states with the same principle quantum number and different angular momentum components (e.g., $2s/2p$ splitting) related to band nonparabolicity, spin-orbit interaction, and deviation of the electron-hole interaction from the pure Coulomb $1/\rho$ law. E_{exch} is the characteristic energy of the exchange electron-hole interaction in the exciton. The condition (7) allows one to introduce rigorously the Coulomb interaction in the first-order $\boldsymbol{k} \cdot \boldsymbol{p}$ scheme. We note, however, that in TMD MLs the exciton binding energy is just a fraction (typically 1/3 to 1/4) of the band gap; therefore, in some cases, the higher-order effects due to the Coulomb interaction should be taken into account. These and other effects related to large exciton binding energy, e.g., a collapse of the ground state [46], are beyond the scope of this work.

A. Exciton wave function

We are interested in the excitons formed by the single-particle Bloch states in the vicinity of the $\boldsymbol{K}_\pm$ edges of the Brillouin zone. Neglecting the Coulomb-interaction induced band mixing, the two-particle Bloch function $\mathcal{U}_\mu(\boldsymbol{\rho}_e, \boldsymbol{\rho}_h)$ can be presented as a product of the electron and hole Bloch functions. For the excitonic state active in σ^+ polarization, $\mu = +1$, the electron Bloch state corresponds to the conduction band c in the $\boldsymbol{K}_+$ valley and the hole state in the valence band v in the $\boldsymbol{K}_-$ valley, because the hole state is obtained from the empty state in the valence band by the time-reversal operation [31,36]. Within the $\boldsymbol{k} \cdot \boldsymbol{p}$ model the Coulomb interaction induces the admixture of the remote bands due to the real space localization of the envelope function and, correspondingly, its spread in the reciprocal, $\boldsymbol{k}$-space. We resort to the standard $\boldsymbol{k} \cdot \boldsymbol{p}$ model presented in Refs. [47–49] which adequately describes the D_{3h} point symmetry of the TMD ML and includes several nearest bands in agreement with density functional theory (DFT) calculations. Disregarding spin and neglecting the spin-orbit interaction, we choose the basis functions for the

bands $c + 2, c, v, v - 3$ (see Ref. [48] for notation) in the $\boldsymbol{K}_+$ valley as follows:

$$\mathcal{U}_{c+2}^{(+)} = \frac{\mathcal{X} - i\mathcal{Y}}{\sqrt{2}}, \qquad \mathcal{U}_{c}^{(+)} = \frac{\mathcal{X} + i\mathcal{Y}}{\sqrt{2}},$$

$$\mathcal{U}_{v}^{(+)} = \mathcal{S}, \qquad \mathcal{U}_{v-3}^{(+)} = \frac{\mathcal{X} - i\mathcal{Y}}{\sqrt{2}}. \tag{8}$$

Here the subscript refers to the band, the superscript denotes the valley, and the arguments are omitted for brevity; the functions $\mathcal{X}$ and $\mathcal{Y}$ transform as the coordinates x and y, respectively; the function $\mathcal{S}$ is invariant. One can see that the valence band, v, is invariant under the point-group transformations of the TMD ML, the conduction band, c, transforms as the state with angular momentum z component being equal to $+1$, and the remote valence and conduction bands $v - 3$ and $c + 2$, respectively, transform as states with angular momentum component -1. The $\boldsymbol{K}_-$ valley states are related to the $\boldsymbol{K}_+$ states by the time-reversal operation, therefore the orbital Bloch functions in $\boldsymbol{K}_-$ valley can be obtained by the complex conjugation of the functions in Eq. (8). The effective Hamiltonian for the K_+ valley in the electron representation has the following form:

$$\mathcal{H}_+ = \begin{pmatrix} E_{c+2} & \gamma_6 k_- & \gamma_4 k_+ & 0 \\ \gamma_6^* k_+ & E_c & \gamma_3 k_- & \gamma_5 k_+ \\ \gamma_4^* k_- & \gamma_3^* k_+ & E_v & \gamma_2 k_- \\ 0 & \gamma_5^* k_- & \gamma_2^* k_+ & E_{v-3} \end{pmatrix}, \tag{9}$$

and in the K_- valley the Hamiltonian is obtained by the substitution [48]

$$\gamma_i \to \gamma_i^*, \quad k_\pm \to -k_\mp. \tag{10}$$

Here $\gamma_2, \ldots, \gamma_6$ are the constants related to the interband matrix elements of the momentum operator, and $k_\pm = k_x \pm i k_y$ are the cyclic components of the wave vector operator $\boldsymbol{k} = -i\partial/\partial\boldsymbol{\rho}_e$ reckoned from the Brillouin zone edge. The diagonal terms $\propto k^2$ caused by the free-electron dispersion and distant band contributions are disregarded. Note that if we choose all orbitals $\mathcal{S}, \mathcal{X}, \mathcal{Y}$ to be real, then all γ parameters are purely imaginary. The Hamiltonian in the hole representation is obtained from Eq. (9) by the time-reversal operation; see Ref. [50] for details.

In the first order in the $\boldsymbol{k} \cdot \boldsymbol{p}$ mixing of the conduction and valence bands with the $c + 2$ and $v - 3$ bands, we obtain the wave functions of the excitons $\Psi_{\boldsymbol{0};v;\pm 1}$ in the form

$$\Psi_{\boldsymbol{0};v;\pm 1} = \Phi_v(\boldsymbol{\rho})\mathcal{U}_\pm(\boldsymbol{\rho}_e,\boldsymbol{\rho}_h) + [\hat{k}_\mp \Phi_v(\boldsymbol{\rho})]\mathcal{W}_\mp(\boldsymbol{\rho}_e,\boldsymbol{\rho}_h) + \cdots. \tag{11}$$

Here "$\cdots$" denotes omitted terms related to the $\boldsymbol{k} \cdot \boldsymbol{p}$ mixing of the c and v bands as well as to the distant bands beyond the $c + 2$, $v - 3$ (these terms are not important for the following),

$$[\hat{k}_\mp \Phi_v(\boldsymbol{\rho})] = -i(\partial/\partial x \mp i\partial/\partial y)\Phi_v(\boldsymbol{\rho}),$$

the two-particle Bloch functions are

$$\mathcal{U}_\pm(\boldsymbol{\rho}_e,\boldsymbol{\rho}_h) = \mathcal{U}_c^{(\pm)}(\boldsymbol{\rho}_e)\tilde{\mathcal{U}}_v^{(\mp)}(\boldsymbol{\rho}_h), \tag{12}$$

where the tilde on top means that the Bloch function is taken in the hole representation [31,36,50], and the auxiliary combinations of Bloch functions are derived within the

first-order perturbation theory as

$$\mathcal{W}_-(\boldsymbol{\rho}_e,\boldsymbol{\rho}_h) = \left(\frac{\gamma_6 \mathcal{U}_{c+2}^{(+)}(\boldsymbol{\rho}_e)}{E_c - E_{c+2}} + \frac{\gamma_5^* \mathcal{U}_{v-3}^{(+)}(\boldsymbol{\rho}_e)}{E_c - E_{v-3}}\right)\tilde{\mathcal{U}}_v^{(-)}(\boldsymbol{\rho}_h)$$
$$+ \mathcal{U}_c^{(+)}(\boldsymbol{\rho}_e)\left(\frac{\gamma_4^* \tilde{\mathcal{U}}_{c+2}^{(-)}(\boldsymbol{\rho}_h)}{E_v - E_{c+2}} + \frac{\gamma_2 \tilde{\mathcal{U}}_{v-3}^{(-)}(\boldsymbol{\rho}_h)}{E_v - E_{v-3}}\right), \tag{13a}$$

$$\mathcal{W}_+(\boldsymbol{\rho}_e,\boldsymbol{\rho}_h) = -\left(\frac{\gamma_6^* \mathcal{U}_{c+2}^{(-)}(\boldsymbol{\rho}_e)}{E_c - E_{c+2}} + \frac{\gamma_5 \mathcal{U}_{v-3}^{(-)}(\boldsymbol{\rho}_e)}{E_c - E_{v-3}}\right)\tilde{\mathcal{U}}_v^{(+)}(\boldsymbol{\rho}_h)$$
$$- \mathcal{U}_c^{(-)}(\boldsymbol{\rho}_e)\left(\frac{\gamma_4 \tilde{\mathcal{U}}_{c+2}^{(+)}(\boldsymbol{\rho}_h)}{E_v - E_{c+2}} + \frac{\gamma_2^* \tilde{\mathcal{U}}_{v-3}^{(+)}(\boldsymbol{\rho}_h)}{E_v - E_{v-3}}\right). \tag{13b}$$

Note that the first lines of Eqs. (13a), (13b) result from the $\boldsymbol{k} \cdot \boldsymbol{p}$ mixing of the electron states while the second lines in Eqs. (13a), (13b) result from the $\boldsymbol{k} \cdot \boldsymbol{p}$ mixing of the hole states; see Appendix for details of the derivation. The functions $\mathcal{W}_\pm$ transform, under operations from the D_{3h} point group, as functions with angular momentum components ± 1. Equation (11) illustrates that the states with the angular momentum components ± 1 and ∓ 2 are indistinguishable in D_{3h} point symmetry. This expression already describes the mixing of excitonic states with different parity, particularly, s- and p-shell states within the same valley. Note that inclusion of other bands, beyond those included in Eq. (8) for the $\boldsymbol{K}_+$ valley and similar ones for $\boldsymbol{K}_-$, yield similar additional terms in auxiliary functions, Eq. (13). From a symmetry point of view these contributions reduce to those taken into account already. Inclusion of these disregarded bands would simply renormalize the mixing constants evaluated below, but not impact our results qualitatively. Moreover, the mixing between the valence and conduction band produces the splitting of p_+ and p_- states within the same valley [38,39], while the mixing of s and p excitons occurs due to the admixture of $c + 2$, $v - 3$ bands.

The mixing is schematically shown in Fig. 3 by the example of the $2p_+$ exciton formed from the electron in the K_+ valley, $\Psi_{\boldsymbol{0};2p_+;+1}$ [panel (a)], and the $2s$ exciton formed from the electron in the K_- valley, $\Psi_{\boldsymbol{0};2s;-1}$ [panel (b)]. The mixing of the conduction band with the $c + 2$ band is shown and the modification of the envelopes $\Phi_{2p_+} \to \Phi_s$ and $\Phi_{2s} \to \Phi_{p_+}$ described by Eq. (11) is sketched. We stress that symmetry-wise the functions demonstrated in panels (a) and (b) are equivalent.

B. Short-range interaction

Our ultimate goal is to describe the mixing of the $\Psi_{\boldsymbol{0};2p_+,+1}$ and $\Psi_{\boldsymbol{0};2s,-1}$, where the electrons belong to different valleys. Such mixing can be enabled by the electron-hole Coulomb interaction. Particularly, its short range part is responsible for the simultaneous intervalley transfer of individual charge carriers forming an exciton. Indeed, as it follows from Eqs. (13) the exciton Bloch functions combinations $\mathcal{W}_\pm$ transform exactly as $\mathcal{U}_\pm$ exciton Bloch functions under all D_{3h} point group transformations. We present the effective Hamiltonian
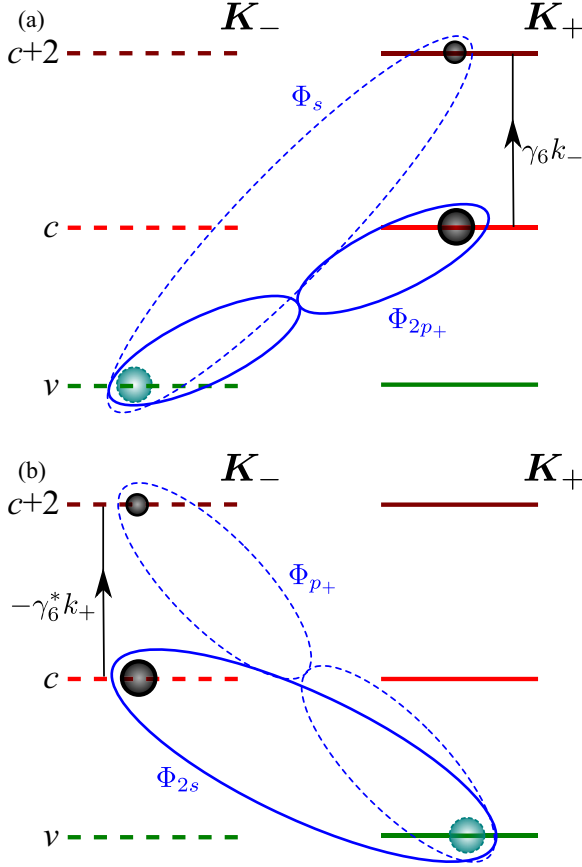
FIG. 3. Schematic illustration of the exciton-state mixing within the same valley, Eqs. (11) and (13). We used here the hole representation for the valence band states. (a) The admixture of the s-shell state to $2p_+$ state in K_+ in $\Psi_{0;2p_+;+1}$. (b) The admixture of the p_+ state to the s-shell state in the K_- valley, $\Psi_{0;2s;-1}$. Black circles denote electron states, green circles denote hole states, and blue solid and dashed lines denote the envelope functions: an "8"-like shape for the p shell and elliptical for the s shell. Vertical arrows denote the matrix elements of $k \cdot p$ Hamiltonians $\mathcal{H}_\pm$ between c and $c+2$ states.

of the short-range electron-hole interaction in the standard form [36]:

$$\mathcal{H}_{sr} = \delta(\boldsymbol{\rho}_e - \boldsymbol{\rho}_h)\, \mathcal{E}_0 a_0^2 \, \hat{V}, \qquad (14)$$

where the Dirac δ function, $\delta(\boldsymbol{\rho}_e - \boldsymbol{\rho}_h)$, acts on the smooth envelopes, $\mathcal{E}_0$ and a_0 are the "atomic" energy scale and the lattice constant, respectively, and the dimensionless matrix $\hat{V}$ acts in the basis of two-particle Bloch functions. It has nonzero elements between the exciton Bloch functions of the same symmetry, e.g., $\langle \mathcal{U}_{c+2}^{(-)} \tilde{\mathcal{U}}_v^{(+)} | \hat{V} | \mathcal{U}_c^{(+)} \tilde{\mathcal{U}}_v^{(-)} \rangle$. Also, taking into account the spin and the spin-orbit interaction, the short-range exchange between the electron and the hole enables simultaneous flip-flop of the electron and hole spins giving rise to the mixing of s-shell and p-shell excitons of the A series.

The calculation shows that the s-p exciton mixing constant β in the Hamiltonian (6) reads

$$\beta_s = \mathcal{E}_0 a_0^3 \Phi_{2s}^*(0) \Phi_{2p}'(0) B_s, \qquad (15)$$

where we introduced the notations

$$\Phi_{2p}'(\rho) = \left(\frac{\partial}{\partial x} - i \frac{\partial}{\partial y} \right) \Phi_{2p_+} = \left(\frac{\partial}{\partial x} + i \frac{\partial}{\partial y} \right) \Phi_{2p_-}, \quad (16)$$

and the dimensionless parameter

$$
\begin{aligned}
B_s = -\frac{1}{a_0} \Bigg(&\frac{\gamma_6 \langle \mathcal{U}_c^{(-)} \tilde{\mathcal{U}}_v^{(+)} | \hat{V} | \mathcal{U}_{c+2}^{(+)} \tilde{\mathcal{U}}_v^{(-)} \rangle}{E_c - E_{c+2}} \\
&+ \frac{\gamma_5^* \langle \mathcal{U}_c^{(-)} \tilde{\mathcal{U}}_v^{(+)} | \hat{V} | \mathcal{U}_{v-3}^{(+)} \tilde{\mathcal{U}}_v^{(-)} \rangle}{E_c - E_{v-3}} \\
&+ \frac{\gamma_4^* \langle \mathcal{U}_c^{(-)} \tilde{\mathcal{U}}_v^{(+)} | \hat{V} | \mathcal{U}_c^{(+)} \tilde{\mathcal{U}}_{c+2}^{(-)} \rangle}{E_v - E_{c+2}} \\
&+ \frac{\gamma_2 \langle \mathcal{U}_c^{(-)} \tilde{\mathcal{U}}_v^{(+)} | \hat{V} | \mathcal{U}_c^{(+)} \tilde{\mathcal{U}}_{v-3}^{(-)} \rangle}{E_v - E_{v-3}} \Bigg).
\end{aligned}
\qquad (17)
$$

Physically, the parameter B_s accounts for the trigonality on the level of Bloch functions. For estimates we obtain from Eq. (15) the short-range contribution to the mixing constant $\beta_s \sim \mathcal{E}_0 (a_0/a_B)^3 B_s$, where a_B is the exciton Bohr radius. As a result, for $\mathcal{E}_0 = 1$ eV, $a_0 = 3$ Å, $a_B = 15$ Å, we have β_s in the range from several tenths to several meV for B_s ranging from 0.1 to 1. In the same way one may roughly estimate that the short-range contribution to the s-shell exciton energy, $\sim \mathcal{E}_0 (a_0/a_B)^2$ is on the order of 10 meV, in reasonable agreement with microscopic calculations [29,40].

C. Exciton oscillator strengths and the long-range exchange interaction

As stated above, the s-p mixing can have a second contribution due to the long-range exchange interaction. The s-shell excitons formed with electrons in $K_\pm$ valley are optically active in $\sigma^\pm$ polarizations [51,52]. These selection rules are described by the dipole moment operator. The reduced matrix elements of the light-matter interaction, $-(\hat{d}_\pm e_\mp)$, where $\hat{d}_\pm = (\hat{d}_x \pm i \hat{d}_y)/\sqrt{2}$, $e_\pm = (e_x \pm i e_y)/\sqrt{2}$ are the circular components of the dipole moment operator and of polarization vector, respectively, can be recast as

$$\langle \Psi_{0;ns;+1} | -(\hat{d}_+ e_-) | 0 \rangle = -\frac{i\sqrt{2}e}{E_{ns}} \Phi_{ns}^*(0) \gamma_3 e_-, \quad (18a)$$

$$\langle \Psi_{0;ns;-1} | -(\hat{d}_- e_+) | 0 \rangle = +\frac{i\sqrt{2}e}{E_{ns}} \Phi_{ns}^*(0) \gamma_3^* e_+, \quad (18b)$$

where E_v is excitation energy of vth exciton. It follows from Eqs. (11) and (13) that the $p_\pm$-shell excitons formed with electrons in $K_\pm$ valley are also optically active, but in the opposite, $\sigma^\mp$, polarizations. The matrix elements of the dipole moment operator evaluated in the first-order in $k \cdot p$ interaction with remote $c+2$, $v-3$ bands take the form

$$\langle \Psi_{0;np_+;+1} | -(\hat{d}_- e_+) | 0 \rangle = -\frac{i\sqrt{2}e}{E_{np}} [\Phi_{np}'(0)]^* \gamma_3 A, \quad (19a)$$

$$\langle \Psi_{0;np_-;-1} | -(\hat{d}_+ e_-) | 0 \rangle = +\frac{i\sqrt{2}e}{E_{np}} [\Phi_{np}'(0)]^* \gamma_3^* A^*, \quad (19b)$$

where

$$A = \frac{1}{i\gamma_3}\left(\frac{\gamma_4\gamma_6^*}{E_{c+2}-E_c} + \frac{\gamma_4\gamma_6^*}{E_{c+2}-E_v}\right.$$
$$\left. - \frac{\gamma_5\gamma_2^*}{E_v - E_{v-3}} - \frac{\gamma_5\gamma_2^*}{E_c - E_{v-3}}\right). \quad (20)$$

Note that inclusion of other distant energy bands would result in additional contributions to the parameter A in Eq. (20). Equations (19) can be conveniently derived taking into account the interband matrix elements of the dipole moment operator contain both $\boldsymbol{k}$-independent and $\boldsymbol{k}$-linear terms as

$$-(\boldsymbol{d}\cdot\boldsymbol{e})^{(+)} = -\frac{i\sqrt{2}e\gamma_3}{E_g}(e_- + iAk_+e_+), \quad (21a)$$

$$-(\boldsymbol{d}\cdot\boldsymbol{e})^{(-)} = +\frac{i\sqrt{2}e\gamma_3^*}{E_g}(e_+ + iA^*k_-e_-), \quad (21b)$$

where the superscript $(\pm)$ denotes the valley where the interband transition takes place.

Hence, for example, both the $2s$-shell exciton formed with the electron in the $\boldsymbol{K}_+$ valley and the $2p_-$-shell exciton formed with the electron in the $\boldsymbol{K}_-$ valley are active in the same polarization. As a result, these state become mixed via the electromagnetic field induced by the excitons. Microscopically, this mixing can be attributed to the long-range exchange interaction between the electron and hole forming the exciton [26,31]. Below we evaluate the mixing both in the electrodynamical and quantum-mechanical approaches and discuss its specifics as compared with the short-range exchange contribution presented above.

For completeness, we note that the s-p exciton mixing due to the short-range interaction, Eq. (15), also produces the nonzero oscillator strength of p-shell excitons. The ratio of the absolute values of matrix elements for excitation of $2p$- and $2s$-excitons can be estimated as $|\beta_s/(E_{2p}-E_{2s})|$ for the short-range mechanism and as $|A|/a_B \sim a_0/a_B$ for the $\boldsymbol{k}\cdot\boldsymbol{p}$ interaction with remote bands. Both ratios are ~ 0.1 depending on the material and environment.

In the framework of the electrodynamical approach we evaluate the interaction of the exciton with the induced electromagnetic field. As before, we focus on $2s$- and $2p$-shell states. It is instructive to consider the excitons propagating with the wave vector $\boldsymbol{K}\parallel x$ in the TMD ML plane excited by the plane wave with the frequency ω, the wave vector components $q_x = K$, $q_y = 0$, $q_z = \sqrt{(n\omega/c)^2 - K^2}$, and the field components $E_{x,y}^0$; n is the effective refraction index of the TMD ML. The exciton-induced field is found from the Maxwell equations [26,31,36]:

$$E_x = E_x^0 + \frac{q_z}{q}iG\left(\frac{|\gamma_3\Phi_{2s}|^2}{\omega_{2s}-\omega-i\Gamma} + \frac{|A\gamma_3\Phi_{2p}'|^2}{\omega_{2p}-\omega-i\Gamma}\right)E_x, \quad (22a)$$

$$E_y = E_y^0 + \frac{q}{q_z}iG\left(\frac{|\gamma_3\Phi_{2s}|^2}{\omega_{2s}-\omega-i\Gamma} + \frac{|A\gamma_3\Phi_{2p}'|^2}{\omega_{2p}-\omega-i\Gamma}\right)E_y, \quad (22b)$$

where to shorten the notations the argument $\rho = 0$ is omitted, $\omega_v = E_v/\hbar$, Γ is the nonradiative damping of the exciton (its difference for the s- and p-shell excitons is disregarded), $q = n\omega/c$, and G is the factor depending of the dielectric surrounding of the TMD ML; it can be expressed via the electromagnetic Greens function. Formally, the mechanical exciton energies in Eqs. (22) should include the contributions of the short-range exchange interaction which already mixes the s- and p-shell states. The analysis of the interference of the short- and long-range exchange mechanisms is beyond the scope of the present paper. From the consistency requirement of Eqs. (22) we obtain the following equations for the exciton eigenfrequencies:

$$(\omega_{2p} - i\Gamma - \lambda_\alpha\Gamma_{0,2p})(\omega_{2s} - i\Gamma - \lambda_\alpha\Gamma_{0,2s}) = -\lambda_\alpha^2\Gamma_{0,2s}\Gamma_{0,2p}, \quad (23)$$

where the subscript $\alpha = x, y$, the factors $\lambda_x = q_z/q$, $\lambda_y = q/q_z$, and we introduced the radiative decay rates of the $2s$- and $2p$-shell excitons as

$$\Gamma_{0,2s} = G|\gamma_3\Phi_{2s}|^2, \quad \Gamma_{0,2p} = G|\gamma_3 A\Phi_{2p}'|^2. \quad (24)$$

Note that the parameter G is real and positive, and $0 < \Gamma_{0,2p} \ll \Gamma_{0,2s}$, the latter inequality holds because with the $\boldsymbol{k}\cdot\boldsymbol{p}$ approach the $|A|/a_B \ll 1$.

Equation (23) demonstrates that the coupling between s- and p-shell excitons is "dissipative" for the states with wave vectors within the light cone, $K < n\omega/c$. Formally this is because for real q_z the right-hand side of Eq. (23) is negative and the coupling constants $\beta_{l,\alpha} = i\lambda_\alpha\hbar\sqrt{\Gamma_{0,2s}\Gamma_{0,2p}}$ are imaginary. Physically, the excitons with $K < n\omega/c$ emit propagating electromagnetic waves, which results in the exciton damping; correspondingly, the mixing between the $2s$ and $2p$ excitons is also associated with their damping. This is quite similar to the situation of the polarization-dependent renormalization of the exciton radiative damping for the s-shell exciton states within the light cone [26,31].

The situation is different for the excitonic states outside the light cone where $K > n\omega/c$. Such excitons do not emit propagating electromagnetic waves and s-p shell state coupling is produced by the curlless (longitudinal) electromagnetic field. Hence, the coupling constants β_α are real and the maximal coupling is achieved for the longitudinal exciton, $\alpha = x$:

$$\beta_{l,x} = \frac{c\hbar K}{n\omega}\Gamma_{0,2s}\frac{|A\Phi_{2p}'|}{|\Phi_{2s}|}, \quad \beta_{l,y} \ll \beta_{l,x}, \quad (25)$$

where we assumed $K \gg n\omega/c$. Note that if the excitons are localized as a whole by a shallow in-plane potential the mixing constant can be estimated by means of Eq. (25) replacing K by the inverse localization length [45].

Equation (25) can be also derived quantum mechanically taking into account the long-range exchange interaction between the electron and the hole. To that end, let us first consider the interband scattering of two electrons from the states $c\boldsymbol{k}_c$ and $v\boldsymbol{k}_v$ to the states $v\boldsymbol{k}_v'$ and $c\boldsymbol{k}_c'$. The matrix element of this process is given by

$$V_{\text{exch}} = \langle\mathcal{U}_{c,\boldsymbol{k}_c'}^{(+)}(\boldsymbol{\rho}_2)\mathcal{U}_{v,\boldsymbol{k}_v'}^{(-)}(\boldsymbol{\rho}_1)|V_c|\mathcal{U}_{c,\boldsymbol{k}_c}^{(-)}(\boldsymbol{\rho}_1)\mathcal{U}_{v,\boldsymbol{k}_v}^{(+)}(\boldsymbol{\rho}_2)\rangle, \quad (26)$$

where $V_c = V_c(\boldsymbol{\rho}_1 - \boldsymbol{\rho}_2)$ is the Coulomb interaction between the electrons. This matrix element differs from the matrix element of the direct interaction by a substitution $\boldsymbol{\rho}_1 \leftrightarrow \boldsymbol{\rho}_2$

in the initial or final state. The specifics of the TMD ML is that the interacting electrons are in different valleys. In contrast to Eqs. (14) and (17), here we are interested in the long-range part of the Coulomb interaction, which allows us to rearrange Eq. (26) as

$$V_{\text{exch}} = \langle \mathcal{U}_{c,\mathbf{k}_c'}^{(+)} | \mathcal{U}_{v,\mathbf{k}_v}^{(+)} \rangle \langle \mathcal{U}_{v,\mathbf{k}_v'}^{(-)} | \mathcal{U}_{c,\mathbf{k}_c}^{(-)} \rangle V_c(\mathbf{k}_c - \mathbf{k}_v') \delta_{\mathbf{k}_c - \mathbf{k}_v', \mathbf{k}_c' - \mathbf{k}_v},$$

(27)

where

$$V_c(\mathbf{K}) = \frac{2\pi e^2}{n^2 K}, \tag{28}$$

is the Fourier image of the Coulomb interaction in 2D. Note that the screening of the long-range exchange interaction is realized by the high-frequency dielectric constant [26]. The overlap integrals of the Bloch functions are nonzero if the $\mathbf{k} \cdot \mathbf{p}$ mixing of the conduction and valence bands is taken into account in the first order, cf. Eq. (13):

$$\langle \mathcal{U}_{c,\mathbf{k}_c'}^{(+)} | \mathcal{U}_{v,\mathbf{k}_v}^{(+)} \rangle = \frac{\gamma_3}{E_g} \left[K_- + iAK_+ \frac{(k_c' + k_v)_+}{2} \right], \quad (29a)$$

$$\langle \mathcal{U}_{v,\mathbf{k}_v'}^{(-)} | \mathcal{U}_{c,\mathbf{k}_c}^{(-)} \rangle = -\frac{\gamma_3}{E_g} \left[K_- + iAK_+ \frac{(k_c' + k_v)_+}{2} \right], \quad (29b)$$

with $\mathbf{K} = \mathbf{k}_c' - \mathbf{k}_v = \mathbf{k}_c - \mathbf{k}_v'$. Evaluation of Eq. (26) by virtue of Eqs. (27) and (29) and transformation to the electron-hole representation yields Eq. (25). Note that to obtain the general expression for the $2s$-$2p$ exciton mixing for the whole range of wave vectors including those within the light cone, one has to take into account the retardation of the Coulomb interaction [53]. To that end it is sufficient to use, instead of Eq. (28), the general form of the retarded potential taken at $z = 0$,

$$V_c = \int_{-\infty}^{\infty} \frac{dk_z}{2\pi} \frac{4\pi e^2}{n^2 [K^2 + k_z^2 - (n\omega/c)^2]}$$

$$= \frac{2\pi e^2}{n^2 \sqrt{K^2 - (n\omega/c)^2}}.$$

For the states within the light cone, $K \to 0$, the efficiency of the dissipative s-p mixing can be estimated according to Eqs. (23) and (24) as $|\beta_l| \sim \hbar\Gamma_{0s}|A|/a_B \sim \hbar\Gamma_{0s}a_0/a_B \sim$ 0.1–1 meV depending on the particular material [54] and dielectric environment, which is close to the estimates in Sec. III B for the short-range mixing mechanism. The coupling constant is enhanced by the factor $K/(n\omega/c) > 1$ for the states outside of the light cone; see Eq. (25).

IV. NONLINEAR OPTICAL PROPERTIES OF EXCITONS IN TMD MLs

In this section we address the consequences of the threefold symmetry of the TMD ML, particularly, the intrinsic exciton mixing on the excitonic nonlinear optical properties; namely, in the two-photon absorption and in the second harmonic generation. It is commonly accepted that the s-shell exciton states are active in single-photon absorption, while p-shell states are active in the two-photon processes [37]. The lack of spatial inversion in TMD MLs enables single-photon
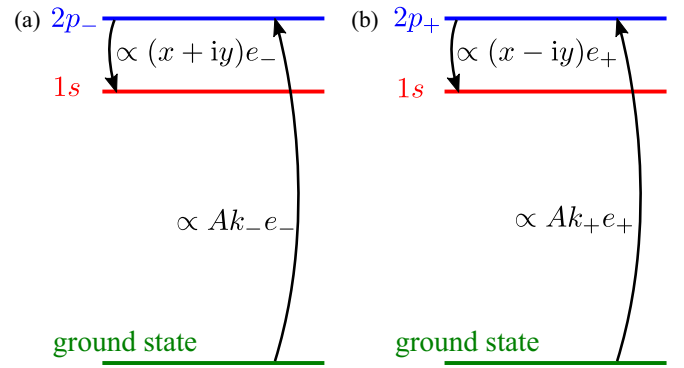

FIG. 4. Demonstration of the two-photon activity of the $1s$ exciton due to $\mathbf{k}$-linear terms in the interband dipole matrix element, Eq. (21). In this mechanism the mixing of excitons is not required. Panels (a) and (b) show the exciton states with the electron in the $\mathbf{K}_-$ and $\mathbf{K}_+$ valley, respectively.

excitation of p-shell excitons and two-photon excitation of s-shell excitons. There are two mechanisms of the selection rules modification: (i) $\mathbf{k}$-linear terms in the interband dipole matrix elements, Eqs. (21), and (ii) the mixing of excitonic states of different parity described by the parameter β in Eq. (6). As a result, each s-shell and p-shell exciton state become simultaneously single- and two-photon active, resulting in the second harmonic generation. Below we consider both mechanisms of the nonlinear excitonic response.

A. Modification of the dipole matrix elements due to $\mathbf{k}$-linear terms

The physical origin of the two-photon excitation of s-shell excitons is illustrated in Fig. 4 for the particular case of the $1s$ exciton. In this two-stage process the single-photon excitation of the $2p$ exciton takes place owing to $\mathbf{k}$-linear terms in Eq. (21). The second photon absorption goes through the interexciton transition [37,55], which changes the envelope function parity $\langle ns|x \mp iy|mp_\pm \rangle \neq 0$. Hence, the s-shell excitonic states $\Psi_{0;ns;+1}$ are excited by two σ^- polarized photons, while the states $\Psi_{0;ns;-1}$ are excited by two σ^+ polarized photons.

Taking into account that the $\mathbf{k}$-linear terms in the interband matrix element result from the $\mathbf{k} \cdot \mathbf{p}$ interaction with remote $c + 2$ and $v - 3$ bands, one can see that the two-photon excitation of s-shell excitons takes place via two "allowed" transitions, i.e., $v \to c + 2$ and $c + 2 \to c$ or $v \to v - 3$ and $v - 3 \to c$. Under the assumptions that the exciton binding energy $E_b \ll E_g$ and that $E_v - E_{v-3}, E_{c+2} - E_c \gg E_g$, the two-photon transition matrix element can be calculated neglecting the Coulomb interaction and averaging over the exciton wave function afterwards. The composite matrix element of the two-photon transition takes the form [56]

$$M^{(2)} = \left(\frac{e}{\omega}\right)^2 \sum_m \frac{(\mathbf{E} \cdot \hat{\mathbf{v}})_{cm}(\mathbf{E} \cdot \hat{\mathbf{v}})_{mv}}{E_m - E_v - \hbar\omega}, \tag{30}$$

where the summation takes place over intermediate states ($m = c + 2$ and $v - 3$ for the $c \to v$ transition), $\hat{\mathbf{v}}$ is the velocity operator, and $\mathbf{E}$ is the complex amplitude of the electric field in the incident wave. For the $c \to v$ two-photon

transition at the K_+ point one has from Eq. (30), neglecting $\hbar\omega = E_g/2$ as compared with $E_v - E_{v-3}, E_{c+2} - E_c$,

$$M^{(2,+)} = \left(\frac{e}{\omega}\right)^2 \frac{i\gamma_3}{\hbar} A E_{\sigma^-}^2, \tag{31}$$

where $E_{\sigma^\mp}$ are the corresponding circular components of the incident field and A is given by Eq. (20). In agreement with the fact that both steps are "allowed," the composite matrix element, Eq. (31), is independent of the wave vector. As a result, s-shell excitons with even envelope functions can be excited in the two-photon process. Similarly to the case of the direct interband transitions, the matrix element of the two-photon excitation of the ns exciton state is given by Eq. (31) multiplied by $\Phi_{ns}^*(0)$ (the normalization area is set to 1):

$$M_{ns}^{(2,+)} = \left(\frac{e}{\omega}\right)^2 \frac{i\gamma_3}{\hbar} A \Phi_{ns}^*(0) E_{\sigma^-}^2. \tag{32}$$

Analogously, one can derive the expression for the matrix element $M_{ns}^{(2,-)}$ of the two-photon excitation by σ^+ polarized light; it differs from Eq. (32) by the replacement of E_{σ^-} by E_{σ^+} and the complex conjugation of the product $i\gamma_3 A$.

The possibility of the two-photon excitation of ns states leads to the electro-dipole second harmonic generation [57]. Phenomenologically, the second harmonic generation in D_{3h} point symmetry is described by the relation [20,58–60]

$$P_x^{(2\omega)} = 2\chi^{(2)} E_x E_y, \quad P_y^{(2\omega)} = \chi^{(2)}\left(E_x^2 - E_y^2\right), \tag{33}$$

Here $\chi^{(2)}$ is the only allowed component of the second-order susceptibility at the normal incidence. For the sake of simplicity we focus on the experimentally relevant case of the second harmonic generation at the $1s$ exciton. Making use of Eqs. (32) and (18) we arrive at the following expression for the susceptibility $\chi^{(2)}$ related with k-linear terms in the dipole matrix elements:

$$\chi_{k,1s}^{(2)} = -\frac{e^3 |\Phi_{1s}(0)|^2}{\omega^2 \omega_{1s}} A \left|\frac{\gamma_3}{\hbar}\right|^2 \frac{1}{2\omega - \omega_{1s} + i\Gamma_{1s}}, \tag{34}$$

where Γ_{1s} is the damping of the $1s$ exciton state. Clearly, $\chi_{k,1s}^{(2)}$ has a resonance at $\omega = \omega_{1s}/2$ where the double frequency corresponds to the $1s$ exciton frequency, in which case the real part of the denominator $2\omega - \omega_{1s} + i\Gamma_{1s}$ vanishes. Analogous expressions for the second-order susceptibility can be derived for ω in the vicinity of any s-shell excitonic resonance.

We note that the two-photon excitation of the p-shell excitons does not require a lack of an inversion center and takes place via a combination of the "allowed" interband and "forbidden" intraband transitions [37,55,61]. Taking into account that the intraband matrix elements of the velocity operator read $v_{cc} = \hbar k/m_c$, $v_{vv} = \hbar k/m_v$, where $m_{c,v}$ are the effective masses of the electron in the conduction and valence bands, respectively, and $1/m_c - 1/m_v = 1/\mu$ where μ is the reduced electron-hole mass, we obtain from Eq. (30)

$$\tilde{M}^{(2,+)} = \left(\frac{e}{\omega}\right)^2 \frac{\gamma_3}{\omega\mu} k_+ E_{\sigma^-}^2. \tag{35}$$

As compared with Eq. (31) for the two-step process involving intra- and interband transitions, the effective two-photon matrix element is linear in the wave vector k. That is why p-shell excitons are optically active in the two-photon processes
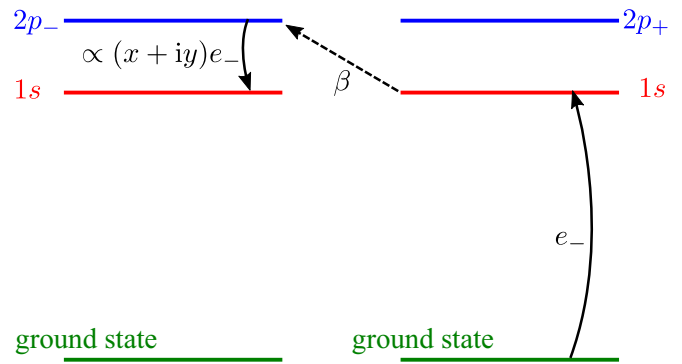

FIG. 5. Demonstration of the two-photon activity of the $1s$ exciton due to the p-s exciton mixing, Eq. (6). Left and right sides show the exciton states with the electron in the K_- and K_+ valley, respectively. Dashed arrows denote the mixing of excitonic states of different parity.

and the matrix element of the two-photon excitation of the mp exciton state is given, in accordance with Eq. (35) by

$$\tilde{M}_{mp}^{(2,+)} = \left(\frac{e}{\omega}\right)^2 \frac{-i\gamma_3}{\omega\mu} [\Phi_{mp}'(0)]^* E_{\sigma^-}^2. \tag{36}$$

Due to the lack of an inversion symmetry, the p-shell excitons are optically active in single photon processes. Taking into account Eqs. (19) we have for the contribution to the susceptibility related to the $2p$ exciton

$$\chi_{k,2p}^{(2)} = \frac{e^3 \hbar |\Phi_{2p}'(0)|^2}{\mu \omega^3 \omega_{2p}} A^* \left|\frac{\gamma_3}{\hbar}\right|^2 \frac{1}{2\omega - \omega_{2p} + i\Gamma_{2p}}. \tag{37}$$

It is worth stressing that the susceptibility is proportional to the parameter A (A^*) responsible for the lack of the inversion center in the TMD ML.

Let us compare the contributions Eq. (34) and (37) to the nonlinear susceptibility at $1s$ and $2p$ excitons. Taking into account that $|\Phi_{2p}'(0)|^2 \sim a_B^{-2} |\Phi_{1s}(0)|^2$ and $\hbar^2/\mu a_B^2 \sim E_b$ we observe that the ratio of the peak values of $\chi^{(2)}$ can be estimated as

$$\frac{\chi_{k,1s}^{(2)}(\omega = \omega_{1s})}{\chi_{k,2p}^{(2)}(\omega = \omega_{2p})} \sim \frac{E_g}{E_b} \frac{\Gamma_{2p}}{\Gamma_{1s}} \gg 1. \tag{38}$$

The dominance of the $1s$ exciton contribution is related to two large factors, $\hbar\omega/E_b \sim E_g/E_b > 1$ and $\Gamma_{2p}/\Gamma_{1s} > 1$, because the broadening of the excited states exceeds by far the broadening of the ground exciton state [20].

B. Mixing of excitons

The mixing of the s- and p-shell excitons described by the Hamiltonian (6) gives rise to additional contributions to the two-photon absorption by s-shell exciton states and to the second-order susceptibility. These nonlinear contributions are similar to those related to the magneto-Stark effect or electric-field induced mixing of excitons in ZnO and GaAs [62,63]. Schematically, one of these contributions is illustrated in Fig. 5: the p-shell exciton can be excited in a one-photon process due to admixture $\propto \beta$ of the s-shell state; the absorption of

the second photon transforms, as in the previous section, the p-shell exciton to the s-shell one.

Microscopically, the response of the TMD ML taking into account the exciton mixing can be derived similarly to the two-photon activity of the $2p$ excitons, because the two-photon excitation of the s-shell state takes place via a combination of the interband and intraband processes. Taking into account that the wave function of the s-shell state contains $\propto \beta$ admixture of the p-shell states, the averaging of Eq. (35) produces a nonzero result for s-shell excitons. Omitting the details of derivation we present the final result for the $1s$ exciton contribution to $\chi^{(2)}$ related to the $1s$-mp exciton mixing:

$$\chi^{(2)}_{\beta,1s} = -\frac{e^3\hbar\Phi_{1s}(0)}{\mu\omega^3\omega_{1s}}\left|\frac{\gamma_3}{\hbar}\right|^2 \sum_m \frac{\beta_{1m}[\Phi'_{mp}(0)]^*}{E_{1s}-E_{mp}}$$
$$\times \frac{1}{2\omega-\omega_{1s}+i\Gamma_{1s}}. \quad (39)$$

The resonance in Eq. (39) takes place, as in Eq. (34), at $\omega = \omega_{1s}/2$ when the second harmonic is resonant with the $1s$ exciton state. Similar expressions can be derived for the contributions to the nonlinear susceptibility $\chi^{(2)}$ in the vicinity of other excitonic resonances. For instance, the second harmonic generation at p-shell excitons is related to the standard mechanism of the two-photon excitation of the p shell, Eq. (36), and single-photon emission from the p exciton due to $\propto \beta$ admixture of the s-shell state to the p-shell state. Here lack of the inversion center is accounted for by the s-p exciton mixing constants β_{1m}.

C. Discussion and comparison with experiment

A giant enhancement of the second harmonic generation at exciton resonances in 1 ML WSe$_2$ flakes has been observed in Ref. [20]. The monolayer samples were obtained by micromechanical cleavage of bulk WSe$_2$ crystal on 90 nm SiO$_2$ on a Si substrate. For the two-photon excitation we use picosecond light pulses, generated by a tunable optical parametric oscillator synchronously pumped by a mode-locked Ti:sapphire laser. The second harmonic emission was collected in reflection geometry; see Ref. [20] for details. Figure 6 demonstrates the intensity of the second harmonic signal as a function of the doubled laser excitation energy. A strong peak at the $1s$ exciton is clearly seen as well as a less prominent feature at the $2s/2p$ excitons. The peaks at exciton resonances in the second-order susceptibility are in agreement with the developed model.

The dominant second harmonic response at the $1s$ exciton state can be explained within the developed model accounting for the modification of the matrix elements, Sec. IV A. The estimates by Eqs. (34) and (38) show that the $1s$ exciton should dominate in the second harmonic emission. Compared with all excited states, the ground exciton has much smaller broadening; moreover, the $2s$ state has much smaller oscillator strength $|\Phi_{2s}(0)/\Phi_{1s}(0)|^2 \ll 1$ already in the hydrogenic model, while, as compared with $2p$ exciton, the enhancement is caused by the factor E_b/E_g. To provide more quantitative comparison we fitted the spectra of the second harmonic generation at $1s$ and $2s/2p$ excitons by Gaussian functions (see black and green profiles in Fig. 6) and extracted the ratio
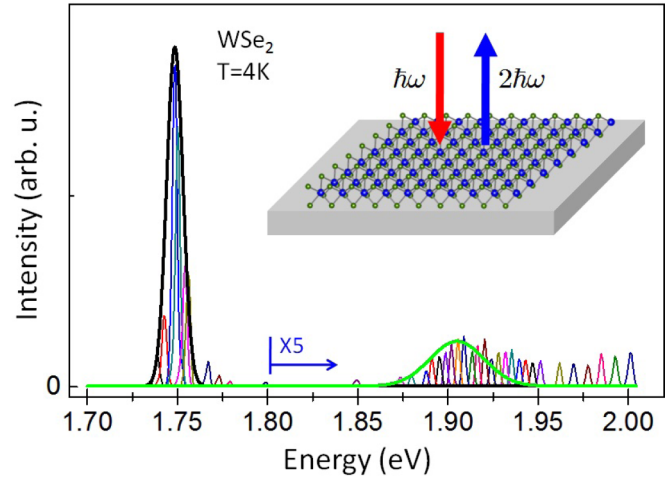

FIG. 6. The second harmonics generation spectrum at $T = 4$ K as function of two-photon energy, $2\hbar\omega$. Narrow peaks represent the emission intensity measured at a given laser frequency. Solid black and green lines represent the fits with Gauss functions to the $1s$ and $2s/2p$ transition profiles. The inset shows the the schematics of the experiment. Adapted from Ref. [20].

of the integral second harmonic intensities at $1s$ and $2s/2p$ states to be about 10. We abstain from more detailed fitting of the experimental data with our model due to uncertainty of the sample parameters and difficulties with evaluation of the overall emission intensity in such samples, cf. [64]. This is in reasonable agreement with the first factor in Eq. (38), $E_g/E_b \sim 5$ in WSe$_2$. It demonstrates that the mechanism related to the modification of selection rules, Eqs. (34) and (37), already reproduces all the main features of the experiment.

Finally, let us emphasize that the interplay of electric- and magnetic-dipole transitions may also result in the second harmonic generation due to simultaneous action of electric and magnetic fields of the light wave (the so-called EB mechanism) as suggested in Ref. [20]. The EB mechanism provides a nonlinear contribution with the same polarization dependence as Eq. (33), which is also enhanced at excitonic resonances. Although many parameters still need to be determined for a meaningful quantitative comparison, we expect at this stage that the EB mechanism is substantially weaker in TMD MLs as compared to the "intrinsic" mechanism suggested here. Indeed, in order to activate the magnetic-dipole transitions at the normal incidence of radiation, the in-plane magnetic field component should play a role. However, its effect is strongly diminished in TMD MLs due to their small thickness. Here the magnetic field has to mix the states related to different bands; this effect is strongly suppressed in atomically thin systems; see, e.g., Ref. [59] for discussion of a similar situation realized in graphene.

V. CONCLUSION

In the present paper we have developed the theory of the excitonic states fine structure in transition metal dichalcogenides monolayers. We have demonstrated that the lack of inversion center in the TMD MLs and their specific threefold rotation symmetry give rise to the mixing of the exciton states with

different parity. In particular, s-shell and p-shell excitonic states whose two-dimensional envelope functions are characterized by the angular momentum components 0 and ± 1 are coupled in TMD MLs. The microscopic theory of the mixing is developed with the $\boldsymbol{k} \cdot \boldsymbol{p}$ formalism. We have identified the origins of the mixing related with the long- and short-range parts of the electron-hole exchange interaction. The estimates show that the coupling constant for the nearest $2s$-$2p$ or $1s$-$2p$ states may be in the range of tenths to units of meV.

The manifestations of the exciton mixing in the linear and, especially, nonlinear optical properties are studied. We have demonstrated that in TMD MLs s-shell excitons are allowed not only in single-photon but also in two-photon processes. Similarly, p-shell excitons are active in single-photon absorption in addition to the two-photon absorption. We have shown that, besides exciton mixing, the lack of the inversion center in TMD MLs results in the modification of optical selection rules, which also provides simultaneous activity of s- and p-shell excitons in one- and two-photon processes. These mechanisms give rise to the effective generation of the crystallographic second harmonics in the electro-dipole approximation. The mechanism related to the modification of the selection rules provides a dominant second harmonic response at the $1s$ exciton resonance, in qualitative agreement with experiment.

The precise evaluation of the exciton oscillator strengths and the nonlinear susceptibility by the combination of the $\boldsymbol{k} \cdot \boldsymbol{p}$ model developed here and the atomistic calculations as well as the studies of the interplay of the exciton mixing in the absence and in the presence of an external electric field are tasks for future studies.

APPENDIX: DERIVATION OF EQS. (11) AND (13)

We start from the electron-hole pair with the wave vectors $\boldsymbol{k}_e$ and $\boldsymbol{k}_h$. The Bloch function of this pair (without the Coulomb interaction) reads

$$\Psi_{\boldsymbol{k}_e, \boldsymbol{k}_h}(\boldsymbol{\rho}_e, \boldsymbol{\rho}_h) = e^{i\boldsymbol{k}_e\boldsymbol{\rho}_e + i\boldsymbol{k}_h\boldsymbol{\rho}_h} \mathcal{U}_{c,\boldsymbol{k}_e}(\boldsymbol{\rho}_e) \tilde{\mathcal{U}}_{v,\boldsymbol{k}_h}(\boldsymbol{\rho}_h). \quad \text{(A1)}$$

Here $\boldsymbol{\rho}_e$ and $\boldsymbol{\rho}_h$ are the in-plane position vectors of the electron and the hole, $\mathcal{U}_{c,\boldsymbol{k}_e}(\boldsymbol{\rho}_e)$ [$\tilde{\mathcal{U}}_{v,\boldsymbol{k}_h}(\boldsymbol{\rho}_h)$] are the single-particle Bloch functions for the conduction band electron (valence band hole). The normalization area is set to unity. In the first order in the $\boldsymbol{k} \cdot \boldsymbol{p}$ mixing we have for the Bloch functions

$$\mathcal{U}_{c,\boldsymbol{k}_e}(\boldsymbol{\rho}_e) = \mathcal{U}_{c,\boldsymbol{k}_e=0}(\boldsymbol{\rho}_e) + \sum_m \mathcal{U}_{m,0}(\boldsymbol{\rho}_e) \frac{\frac{\hbar}{m_0}\langle m|\boldsymbol{k}_e \cdot \boldsymbol{p}|c\rangle}{E_c - E_m},$$
$$\text{(A2)}$$

$$\tilde{\mathcal{U}}_{v,\boldsymbol{k}_h}(\boldsymbol{\rho}_e) = \tilde{\mathcal{U}}_{v,\boldsymbol{k}_h=0}(\boldsymbol{\rho}_e) + \sum_n \tilde{\mathcal{U}}_{n,0}(\boldsymbol{\rho}_e) \frac{\frac{\hbar}{m_0}\langle n|\boldsymbol{k}_h \cdot \boldsymbol{p}|c\rangle}{E_c - E_n}.$$
$$\text{(A3)}$$

The wave vectors are reckoned from the corresponding $\boldsymbol{K}$ point of the Brillouin zone; e.g., $\boldsymbol{k}_e = 0$ corresponds to $\boldsymbol{K}_+$ valley for the electron and $\boldsymbol{k}_h = 0$ corresponds to the $\boldsymbol{K}_-$ valley for the hole in the electron-hole pair excited by the σ^+ light.

Now we account for the excitonic effect. We assume that the exciton binding energy is small compared to the bandgaps and include the Coulomb correlation in the form

$$\Psi_{exc}(\boldsymbol{\rho}_e, \boldsymbol{\rho}_h) = \sum_{\boldsymbol{k}_e, \boldsymbol{k}_h} C_{\boldsymbol{k}_e, \boldsymbol{k}_h} e^{i\boldsymbol{k}_e\boldsymbol{\rho}_e + i\boldsymbol{k}_h\boldsymbol{\rho}_h} \mathcal{U}_{c,\boldsymbol{k}_e}(\boldsymbol{\rho}_e) \tilde{\mathcal{U}}_{v,\boldsymbol{k}_h}(\boldsymbol{\rho}_h). \quad \text{(A4)}$$

Here $C_{\boldsymbol{k}_e, \boldsymbol{k}_h}$ is the Fourier transform of the exciton envelope function calculated within the effective mass approach,

$$\exp(i\boldsymbol{K}\boldsymbol{R})\Phi(\boldsymbol{\rho}_e - \boldsymbol{\rho}_h) = \sum_{\boldsymbol{k}_e, \boldsymbol{k}_h} C_{\boldsymbol{k}_e, \boldsymbol{k}_h} e^{i\boldsymbol{k}_e\boldsymbol{\rho}_e + i\boldsymbol{k}_h\boldsymbol{\rho}_h}. \quad \text{(A5)}$$

Hence, in the first order in the $\boldsymbol{k} \cdot \boldsymbol{p}$ mixing one has

$$\Psi_{exc}(\boldsymbol{\rho}_e, \boldsymbol{\rho}_h)$$
$$= \sum_{\boldsymbol{k}_e, \boldsymbol{k}_h} C_{\boldsymbol{k}_e, \boldsymbol{k}_h} e^{i\boldsymbol{k}_e\boldsymbol{\rho}_e + i\boldsymbol{k}_h\boldsymbol{\rho}_h} \mathcal{U}_{c,0}(\boldsymbol{\rho}_e) \tilde{\mathcal{U}}_{v,0}(\boldsymbol{\rho}_h)$$
$$+ \delta\Psi_e(\boldsymbol{\rho}_e) \tilde{\mathcal{U}}_{v,0}(\boldsymbol{\rho}_h) + \delta\Psi_h(\boldsymbol{\rho}_h) \mathcal{U}_{c,0}(\boldsymbol{\rho}_e). \quad \text{(A6)}$$

Making use of Eq. (A2), we have for $\delta\Psi_e$

$$\delta\Psi_e(\boldsymbol{\rho}_e) = \sum_{\boldsymbol{k}_e, \boldsymbol{k}_h} C_{\boldsymbol{k}_e, \boldsymbol{k}_h} e^{i\boldsymbol{k}_e\boldsymbol{\rho}_e + i\boldsymbol{k}_h\boldsymbol{\rho}_h} \sum_m \mathcal{U}_{m,0}(\boldsymbol{\rho}_e)$$
$$\times \frac{\frac{\hbar}{m_0}\langle m|\boldsymbol{k}_e \cdot \boldsymbol{p}|c\rangle}{E_c - E_m}$$
$$= \sum_{\boldsymbol{k}_e, \boldsymbol{k}_h} C_{\boldsymbol{k}_e, \boldsymbol{k}_h} e^{i\boldsymbol{k}_e\boldsymbol{\rho}_e + i\boldsymbol{k}_h\boldsymbol{\rho}_h} k_-^{(e)}$$
$$\times \left[\frac{\gamma_6 \mathcal{U}_{c+2}^{(e)}(\boldsymbol{\rho}_e)}{E_c - E_{c+2}} + \frac{\gamma_5^* \mathcal{U}_{v-3}^{(e)}(\boldsymbol{\rho}_e)}{E_c - E_{v-3}} \right]. \quad \text{(A7)}$$

In the latter equality we have considered the particular case of the electron in the $\boldsymbol{K}_+$ valley and taken into account two admixed bands, $c + 2$ and $v - 3$, where

$$\frac{\hbar}{m_0}\langle c+2|\boldsymbol{k}_e \cdot \boldsymbol{p}|c\rangle = \gamma_6 k_-^{(e)}, \quad \frac{\hbar}{m_0}\langle v-3|\boldsymbol{k}_e \cdot \boldsymbol{p}|c\rangle = \gamma_5^* k_-^{(e)}.$$

To sum over $\boldsymbol{k}_e, \boldsymbol{k}_h$ in Eq. (A7) we consider the exciton with the center-of-mass wave vector $\boldsymbol{K} = 0$ and make use of Eq. (A5) to obtain

$$\sum_{\boldsymbol{k}_e, \boldsymbol{k}_h} C_{\boldsymbol{k}_e, \boldsymbol{k}_h} e^{i\boldsymbol{k}_e\boldsymbol{\rho}_e + i\boldsymbol{k}_h\boldsymbol{\rho}_h} k_-^{(e)}$$
$$= \sum_{\boldsymbol{k}_e, \boldsymbol{k}_h} C_{\boldsymbol{k}_e, \boldsymbol{k}_h}(-i)\left(\frac{\partial}{\partial x_e} - i\frac{\partial}{\partial y_e}\right)e^{i\boldsymbol{k}_e\boldsymbol{\rho}_e + i\boldsymbol{k}_h\boldsymbol{\rho}_h}$$
$$= -i\left(\frac{\partial}{\partial x_e} - i\frac{\partial}{\partial y_e}\right)\Phi(\boldsymbol{\rho}_e - \boldsymbol{\rho}_h) = \hat{k}_-\Phi(\boldsymbol{\rho}). \quad \text{(A8)}$$

Combining Eqs. (A6), (A7), and (A8) we obtain Eq. (10) of the paper with the function $\mathcal{W}_-$ in the form

$$\mathcal{W}_- = \left(\frac{\gamma_6 \mathcal{U}_{c+2}^{(+)}(\boldsymbol{\rho}_e)}{E_c - E_{c+2}} + \frac{\gamma_5^* \mathcal{U}_{v-3}^{(+)}(\boldsymbol{\rho}_e)}{E_c - E_{v-3}}\right)\tilde{\mathcal{U}}_v^{(-)}(\boldsymbol{\rho}_h).$$

This is the first line of Eq. (13a). The second line of Eq. (13a) can be derived in the same way from $\delta\Psi_h$ in Eq. (A6).

[1] K. F. Mak, C. Lee, J. Hone, J. Shan, and T. F. Heinz, Atomically Thin MoS$_2$: A New Direct-Gap Semiconductor, Phys. Rev. Lett. **105**, 136805 (2010).

[2] D. Xiao, G.-B. Liu, W. Feng, X. Xu, and W. Yao, Coupled Spin and Valley Physics in Monolayers of MoS$_2$ and Other Group-VI Dichalcogenides, Phys. Rev. Lett. **108**, 196802 (2012).

[3] Q. H. Wang, K. Kalantar-Zadeh, A. Kis, J. N. Coleman, and M. S. Strano, Electronics and optoelectronics of two-dimensional transition metal dichalcogenides, Nat. Nano. **7**, 699 (2012).

[4] G.-B. Liu, D. Xiao, Y. Yao, X. Xu, and W. Yao, Electronic structures and theoretical modelling of two-dimensional group-VIB transition metal dichalcogenides, Chem. Soc. Rev. **44**, 2643 (2015).

[5] A. V. Kolobov and J. Tominaga, *Two-Dimensional Transition-Metal Dichalcogenides* (Springer, Berlin, 2016).

[6] H. Yu, X. Cui, X. Xu, and W. Yao, Valley excitons in two-dimensional semiconductors, Nat. Sci. Rev. **2**, 57 (2015).

[7] G. Moody, J. Schaibley, and X. Xu, Exciton dynamics in monolayer transition metal dichalcogenides, J. Opt. Soc. Am. B **33**, C39 (2016).

[8] A. V. Chaplik and M. V. Entin, Charged impurities in very thin layers, J. Exp. Theor. Phys. **34**, 1335 (1972).

[9] L. V. Keldysh, Coulomb interaction in thin semiconductor and semimetal films, JETP Lett. **29**, 658 (1979).

[10] T. Cheiwchanchamnangij and W. R. L. Lambrecht, Quasiparticle band structure calculation of monolayer, bilayer, and bulk MoS$_2$, Phys. Rev. B **85**, 205302 (2012).

[11] A. Ramasubramaniam, Large excitonic effects in monolayers of molybdenum and tungsten dichalcogenides, Phys. Rev. B **86**, 115409 (2012).

[12] H. Shi, H. Pan, Y.-W. Zhang, and B. I. Yakobson, Quasiparticle band structures and optical properties of strained monolayer MoS$_2$ and WS$_2$, Phys. Rev. B **87**, 155304 (2013).

[13] D. Y. Qiu, F. H. da Jornada, and S. G. Louie, Optical Spectrum of MoS$_2$ Many-Body Effects and Diversity of Exciton States, Phys. Rev. Lett. **111**, 216805 (2013).

[14] G. Berghäuser and E. Malic, Analytical approach to excitonic properties of MoS$_2$, Phys. Rev. B **89**, 125309 (2014).

[15] K. F. Mak, K. He, C. Lee, G. H. Lee, J. Hone, T. F. Heinz, and J. Shan, Tightly bound trions in monolayer MoS$_2$, Nat. Mater. **12**, 207 (2013).

[16] K. He, N. Kumar, L. Zhao, Z. Wang, K. F. Mak, H. Zhao, and J. Shan, Tightly Bound Excitons in Monolayer WSe$_2$, Phys. Rev. Lett. **113**, 026803 (2014).

[17] A. Chernikov, T. C. Berkelbach, H. M. Hill, A. Rigosi, Y. Li, O. B. Aslan, D. R. Reichman, M. S. Hybertsen, and T. F. Heinz, Exciton Binding Energy and Nonhydrogenic Rydberg Series in Monolayer WS$_2$, Phys. Rev. Lett. **113**, 076802 (2014).

[18] Z. Ye, T. Cao, K. O'Brien, H. Zhu, X. Yin, Y. Wang, S. G. Louie, and X. Zhang, Probing excitonic dark states in single-layer tungsten disulphide, Nature (London) **513**, 214 (2014).

[19] A. R. Klots, A. K. M. Newaz, B. Wang, D. Prasai, H. Krzyzanowska, J. Lin, D. Caudel, N. J. Ghimire, J. Yan, B. L. Ivanov, K. A. Velizhanin, A. Burger, D. G. Mandrus, N. H. Tolk, S. T. Pantelides, and K. I. Bolotin, Probing excitonic states in suspended two-dimensional semiconductors by photocurrent spectroscopy, Sci. Rep. **4**, 6608 (2014).

[20] G. Wang, X. Marie, I. Gerber, T. Amand, D. Lagarde, L. Bouet, M. Vidal, A. Balocchi, and B. Urbaszek, Giant Enhancement of the Optical Second-Harmonic Emission of WSe$_2$ Monolayers by

Laser Excitation at Exciton Resonances, Phys. Rev. Lett. **114**, 097403 (2015).

[21] T. Korn, S. Heydrich, M. Hirmer, J. Schmutzler, and C. Schüller, Low-temperature photocarrier dynamics in monolayer MoS$_2$, Appl. Phys. Lett. **99**, 102109 (2011).

[22] G. Wang, L. Bouet, D. Lagarde, M. Vidal, A. Balocchi, T. Amand, X. Marie, and B. Urbaszek, Valley dynamics probed through charged and neutral exciton emission in monolayer WSe$_2$, Phys. Rev. B **90**, 075413 (2014).

[23] M. Palummo, M. Bernardi, and J. C. Grossman, Exciton radiative lifetimes in layered transition metal dichalcogenides, Nano Lett. **15**, 2794 (2015).

[24] C. Poellmann, P. Steinleitner, U. Leierseder, P. Nagler, G. Plechinger, M. Porer, R. Bratschitsch, C. Schuller, T. Korn, and R. Huber, Resonant internal quantum transitions and femtosecond radiative decay of excitons in monolayer WSe$_2$, Nat. Mater. **14**, 889 (2015).

[25] C. Robert, D. Lagarde, F. Cadiz, G. Wang, B. Lassagne, T. Amand, A. Balocchi, P. Renucci, S. Tongay, B. Urbaszek, and X. Marie, Exciton radiative lifetime in transition metal dichalcogenide monolayers, Phys. Rev. B **93**, 205423 (2016).

[26] M. M. Glazov, T. Amand, X. Marie, D. Lagarde, L. Bouet, and B. Urbaszek, Exciton fine structure and spin decoherence in monolayers of transition metal dichalcogenides, Phys. Rev. B **89**, 201302(R) (2014).

[27] T. Yu and M. W. Wu, Valley depolarization due to intervalley and intravalley electron-hole exchange interactions in monolayer MoS$_2$, Phys. Rev. B **89**, 205303 (2014).

[28] H. Yu, G.-B. Liu, P. Gong, X. Xu, and W. Yao, Dirac cones and Dirac saddle points of bright excitons in monolayer transition metal dichalcogenides, Nat. Commun. **5**, 3876 (2014).

[29] D. Y. Qiu, T. Cao, and S. G. Louie, Nonanalyticity, Valley Quantum Phases, and Lightlike Exciton Dispersion in Monolayer Transition Metal Dichalcogenides: Theory and First-Principles Calculations, Phys. Rev. Lett. **115**, 176801 (2015).

[30] C. R. Zhu, K. Zhang, M. Glazov, B. Urbaszek, T. Amand, Z. W. Ji, B. L. Liu, and X. Marie, Exciton valley dynamics probed by Kerr rotation in WSe$_2$ monolayers, Phys. Rev. B **90**, 161302 (2014).

[31] M. M. Glazov, E. L. Ivchenko, G. Wang, T. Amand, X. Marie, B. Urbaszek, and B. L. Liu, Spin and valley dynamics of excitons in transition metal dichalcogenide monolayers, Phys. Status Solidi B **252**, 2349 (2015).

[32] K. L. Seyler, J. R. Schaibley, P. Gong, P. Rivera, A. M. Jones, S. Wu, J. Yan, D. G. Mandrus, W. Yao, and X. Xu, Electrical control of second-harmonic generation in a WSe$_2$ monolayer transistor, Nat. Nanotechnol. **10**, 407 (2015).

[33] M. L. Trolle, Y.-C. Tsao, K. Pedersen, and T. G. Pedersen, Observation of excitonic resonances in the second harmonic spectrum of MoS$_2$, Phys. Rev. B **92**, 161409 (2015).

[34] M. L. Trolle, G. Seifert, and T. G. Pedersen, Theory of excitonic second-harmonic generation in monolayer MoS$_2$, Phys. Rev. B **89**, 235410 (2014).

[35] M. Grüning and C. Attaccalite, Second harmonic generation in h-BN and MoS$_2$ monolayers: Role of electron-hole interaction, Phys. Rev. B **89**, 081102 (2014).

[36] E. L. Ivchenko, *Optical Spectroscopy of Semiconductor Nanostructures* (Alpha Science, Harrow, UK, 2005).

[37] T. C. Berkelbach, M. S. Hybertsen, and D. R. Reichman, Bright and dark singlet excitons via linear and two-photon spectroscopy

in monolayer transition-metal dichalcogenides, Phys. Rev. B **92**, 085413 (2015).

[38] A. Srivastava and A. Imamoglu, Signatures of Bloch-Band Geometry on Excitons: Nonhydrogenic Spectra in Transition-Metal Dichalcogenides, Phys. Rev. Lett. **115**, 166802 (2015).

[39] J. Zhou, W.-Y. Shan, W. Yao, and D. Xiao, Berry Phase Modification to the Energy Spectrum of Excitons, Phys. Rev. Lett. **115**, 166803 (2015).

[40] J. P. Echeverry, B. Urbaszek, T. Amand, X. Marie, and I. C. Gerber, Splitting between bright and dark excitons in transition metal dichalcogenide monolayers, Phys. Rev. B **93**, 121107 (2016).

[41] A. O. Slobodeniuk and D. M. Basko, Spin-flip processes and radiative decay of dark intravalley excitons in transition metal dichalcogenide monolayers, 2D Mat. **3**, 035009 (2016).

[42] G. F. Koster, R. G. Wheeler, J. O. Dimmock, and H. Statz, *Properties of the Thirty-Two Point Groups* (MIT Press, Cambridge, MA, 1963).

[43] F. Wu, F. Qu, and A. H. MacDonald, Exciton band structure of monolayer MoS$_2$, Phys. Rev. B **91**, 075310 (2015).

[44] M. Trushin, M. O. Goerbig, and W. Belzig, Optical absorption by Dirac excitons in single-layer transition-metal dichalcogenides, Phys. Rev. B **94**, 041301 (2016).

[45] M. M. Glazov, E. L. Ivchenko, R. von Baltz, and E. G. Tsitsishvili, Fine structure of excited excitonic states in quantum dots, Int. J. Nanosci. **6**, 265 (2007).

[46] T. Stroucken, S. W. Koch, Optically bright *p*-excitons indicating strong Coulomb coupling in transition-metal dichalcogenides, J. Phys. Condes. Matter **27**, 345003 (2015).

[47] A. Kormányos, V. Zólyomi, N. D. Drummond, P. Rakyta, G. Burkard, and V. I. Fal'ko, Monolayer MoS$_2$: Trigonal warping, the γ valley, and spin-orbit coupling effects, Phys. Rev. B **88**, 045416 (2013).

[48] A. Kormanyos, G. Burkard, M. Gmitra, J. Fabian, V. Zólyomi, N. D. Drummond, and V. Fal'ko, $\boldsymbol{k} \cdot \boldsymbol{p}$ theory for two-dimensional transition metal dichalcogenide semiconductors, 2D Mater. **2**, 022001 (2015).

[49] G. Wang, L. Bouet, M. M. Glazov, T. Amand, E. L. Ivchenko, E. Palleau, X. Marie, and B. Urbaszek, Magneto-optics in transition metal diselenide monolayers, 2D Mater. **2**, 034002 (2015).

[50] G. L. Bir, G. E. Pikus, *Symmetry and Strain-induced Effects in Semiconductors* (Wiley/Halsted, New York, 1974).

[51] K. F. Mak, K. He, J. Shan, and T. F. Heinz, Control of valley polarization in monolayer MoS$_2$ by optical helicity, Nat. Nanotechnol. **7**, 494 (2012).

[52] G. Sallen, L. Bouet, X. Marie, G. Wang, C. R. Zhu, W. P. Han, Y. Lu, P. H. Tan, T. Amand, B. L. Liu, and B. Urbaszek, Robust optical emission polarization in MoS$_2$ monolayers through selective valley excitation, Phys. Rev. B **86**, 081301 (2012).

[53] S. V. Goupalov, E. L. Ivchenko, and A. V. Kavokin, Fine structure of localized exciton levels in quantum wells, J. Exp. Theor. Phys. **86**, 388 (1998).

[54] D. V. Rybkovskiy, I. C. Gerber, and M. V. Durnev, Atomically inspired $k \cdot p$ approach and valley Zeeman effect in transition metal dichalcogenide monolayers, arXiv:1610.02695.

[55] G. D. Mahan, Theory of two-photon spectroscopy in solids, Phys. Rev. **170**, 825 (1968).

[56] E. L. Ivchenko, Two-photon absorption and optical orientation of free carriers in cubic crystals, Sov. Phys. Solid State **14**, 2942 (1973).

[57] T. G. Pedersen, H. D. Cornean, Optical second harmonic generation from Wannier excitons, Europhys. Lett. **78**, 27005 (2007).

[58] L. E. Golub, S. A. Tarasenko, M. V. Entin, and L. I. Magarill, Valley separation in graphene by polarized light, Phys. Rev. B **84**, 195408 (2011).

[59] M.M. Glazov and S.D. Ganichev, High frequency electric field induced nonlinear effects in graphene, Phys. Rep. **535**, 101 (2014).

[60] L. E. Golub and S. A. Tarasenko, Valley polarization induced second harmonic generation in graphene, Phys. Rev. B **90**, 201402 (2014).

[61] For the same reason, the two-photon excitation efficiency of *s*-shell excitons is parametrically smaller than that of *p*-shell excitons. Therefore, the two-photon photoluminescence excitation is dominated by 2*p*-exciton transitions.

[62] M. Lafrentz, D. Brunne, B. Kaminski, V. V. Pavlov, A. V. Rodina, R. V. Pisarev, D. R. Yakovlev, A. Bakin, and M. Bayer, Magneto-Stark Effect of Excitons as the Origin of Second Harmonic Generation in ZnO, Phys. Rev. Lett. **110**, 116402 (2013).

[63] D. Brunne, M. Lafrentz, V. V. Pavlov, R. V. Pisarev, A. V. Rodina, D. R. Yakovlev, and M. Bayer, Electric field effect on optical harmonic generation at the exciton resonances in GaAs, Phys. Rev. B **92**, 085202 (2015).

[64] D.-H. Lien, J. S. Kang, M. Amani, K. Chen, M. Tosun, H.-P. Wang, T. Roy, M. S. Eggleston, M. C. Wu, M. Dubey, S.-C. Lee, J.-H. He, and A. Javey, Engineering light outcoupling in 2D materials, Nano Lett. **15**, 1356 (2015).